

# High-Performance Deep Ultraviolet Photodetector Based on a One-Dimensional Lead-Free Halide Perovskite CsCu<sub>2</sub>I<sub>3</sub> Film with High Stability

Jie Yang,<sup>▽</sup> Wei Kang,<sup>▽</sup> Zhengzheng Liu,<sup>▽</sup> Mingyu Pi, Lin-Bao Luo, Chen Li, Hao Lin, Zhongtao Luo, Juan Du,<sup>\*</sup> Miao Zhou,<sup>\*</sup> and Xiaosheng Tang<sup>\*</sup>

**Cite This:** *J. Phys. Chem. Lett.* 2020, 11, 6880–6886

**Read Online**

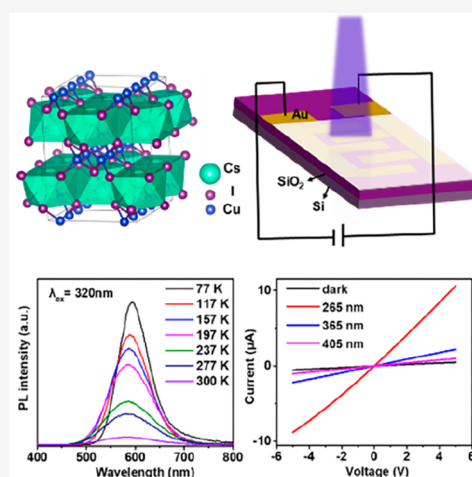
ACCESS |

Metrics & More

Article Recommendations

Supporting Information

**ABSTRACT:** Lead halide perovskites have received much attention in the field of optoelectronic devices. However, the environment-unfriendly nature and intrinsic instability of these perovskites hamper their commercial applications. In this work, one novel one-dimensional lead-free halide perovskite with high stability, CsCu<sub>2</sub>I<sub>3</sub>, was prepared via an antisolvent-assisted crystallization method. The prepared CsCu<sub>2</sub>I<sub>3</sub> bears a high exciton binding energy of ~105 meV and a high photoluminescence quantum yield of 12.3%. We fabricated a deep ultraviolet photodetector based on a CsCu<sub>2</sub>I<sub>3</sub> film that is nearly blind to 405 nm visible light but is sensitive to 265 and 365 nm illumination. The device exhibits excellent reproducibility and a high  $I_{\text{light}}/I_{\text{dark}}$  ratio of 22 under 265 nm illumination. Furthermore, the responsivity, specific detectivity, and external quantum efficiency are as high as 22.1 mA/W,  $1.2 \times 10^{11}$  Jones, and 10.3% under a light density of 0.305 mW/cm<sup>2</sup>, respectively. These findings demonstrate that CsCu<sub>2</sub>I<sub>3</sub> perovskites should have great potential for future optoelectronics.



Recently, UV photodetectors have gained tremendous research interest in industrial and scientific applications, including but not limited to UV radiation dosimetry, chemical sensing, and astronomical observation.<sup>1–6</sup> In the past few years, a series of UV photodetectors based on wide-band-gap semiconductors (e.g., zinc oxide, diamond, and AlGaN) have been explored.<sup>7–10</sup> However, their development was severely impeded by complex manufacturing technology, high operation voltage, and mechanical inflexibility. It is desirable to explore alternative materials for highly sensitive UV photodetectors.

Halide perovskites, which have high carrier mobilities, large absorption coefficients, and low-cost solution processability, have been proposed as ideal candidates for UV photodetectors.<sup>11–16</sup> For instance, Sargent's group presented a novel MAPbCl<sub>3</sub> single crystal UV photodetector with a large responsivity of 46.9 mA/W and rapid response ( $\tau_{\text{rise}}/\tau_{\text{decay}} = 24$  ms/62 ms).<sup>11</sup> Fang's group reported a UV photodetector consisting of CsPbCl<sub>3</sub> microplatelets that exhibited remarkable optoelectronic properties in terms of responsivity (0.45 A/W) and detectivity ( $10^{11}$  Jones).<sup>13</sup> However, Pb-based perovskites usually suffer from environmental unfriendliness and intrinsic instability, which restrict their practical applications.

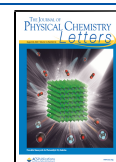
In the present work, we successfully synthesized a high-quality one-dimensional (1D) lead-free perovskite CsCu<sub>2</sub>I<sub>3</sub>

film using an antisolvent-assisted crystallization method. The 1D crystal structure and soft crystal lattice facilitate the formation of self-trapped excitons, which emit at 580 nm with a large Stokes shift. Emphatically, the CsCu<sub>2</sub>I<sub>3</sub> film exhibits bright yellow emission with a high photoluminescence quantum yield (PLQY) of up to 12.3% and excellent stability. For the first time, we fabricated a deep UV (DUV) photodetector based on the CsCu<sub>2</sub>I<sub>3</sub> film. Remarkably, the device exhibits apparent sensitivity to 265 and 365 nm illumination but is nearly blind to 405 nm visible light. The photocurrent/dark current ( $I_{\text{light}}/I_{\text{dark}}$ ) ratio is as high as 22 at a bias of 3 V under 265 nm illumination. Furthermore, the responsivity ( $R$ ), specific detectivity ( $D^*$ ), and external quantum efficiency (EQE) are as high as 22.1 mA/W,  $1.2 \times 10^{11}$  Jones, and 10.3% under a light density of 0.305 mW/cm<sup>2</sup>, respectively. These results suggest that the 1D perovskite

**Received:** June 13, 2020

**Accepted:** July 6, 2020

**Published:** July 6, 2020



CsCu<sub>2</sub>I<sub>3</sub> would be a promising candidate for future DUV optoelectronic applications.

Figure 1a,b shows the crystal structure of CsCu<sub>2</sub>I<sub>3</sub>, which has a 1D ribbonlike structure and belongs to the orthorhombic

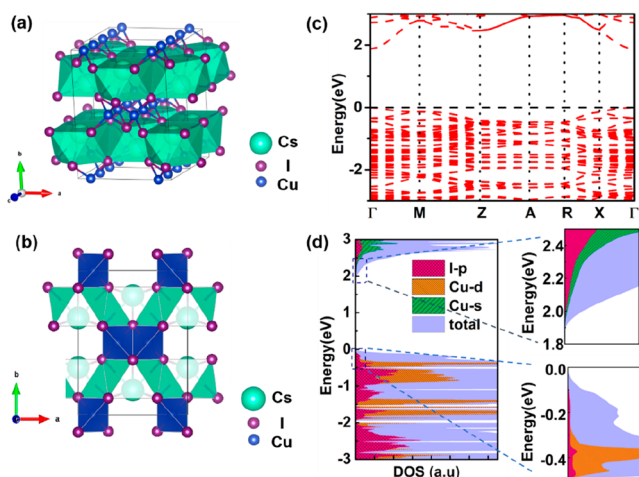


**Figure 1.** (a) Crystal structure of CsCu<sub>2</sub>I<sub>3</sub>. (b) CsCu<sub>2</sub>I<sub>3</sub> structure viewed along the *c* axis. (c) Calculated band structures and (d) partial DOS of CsCu<sub>2</sub>I<sub>3</sub> projected onto different orbitals of the I and Cu atoms.

space group *Cmcm* with unit cell dimensions of  $a = 10.51 \text{ \AA}$ ,  $b = 13.15 \text{ \AA}$ ,  $c = 6.07 \text{ \AA}$ ,  $\alpha = \beta = \gamma = 90^\circ$ , and  $V = 838.6 \text{ \AA}^3$ . The edge-sharing [Cu<sub>2</sub>I<sub>3</sub>]<sup>-</sup> anionic ribbon is spatially surrounded and isolated by Cs<sup>+</sup> atoms.<sup>17–19</sup> In order to gain insight into its electronic properties, we performed density functional theory (DFT)-based first-principles calculations focusing on the band structure and density of states (DOS). As shown in Figure 1c,d, CsCu<sub>2</sub>I<sub>3</sub> has a direct band gap of 1.9 eV at the  $\Gamma$  point. The conduction band minimum (CBM) of CsCu<sub>2</sub>I<sub>3</sub> is mainly composed of Cu 4s and I 5p orbitals, while the valence band maximum (VBM) mainly involves hybrid orbitals of Cu 3d and I 5p. We notice little contribution of the Cs<sup>+</sup> ion to either the CBM or VBM because of the small number of *s* orbitals. Meanwhile, we find that the valence band edge contributed by Cu 4s and I 5p orbitals is relatively flat, while the Cu 3d- and I 5p-dominated conduction band edge is quite dispersive, indicating different effective masses for electrons and holes.

The CsCu<sub>2</sub>I<sub>3</sub> film was synthesized using an antisolvent-assisted crystallization method.<sup>20–22</sup> The crystal structure of the CsCu<sub>2</sub>I<sub>3</sub> film was confirmed by X-ray diffraction (XRD) analysis (Figure 2a). The strong diffraction peaks at 11.2°, 22.1°, and 26.7°, assigned to the (110), (220), and (221) planes, confirmed that the obtained CsCu<sub>2</sub>I<sub>3</sub> film had the orthorhombic CsCu<sub>2</sub>I<sub>3</sub> crystal structure in space group *Cmcm* (JCPDS no. 77-0069),<sup>19,23,24</sup> and did not contain impurities. Figure 2b shows the scanning electron microscopy (SEM) image of the CsCu<sub>2</sub>I<sub>3</sub> film on a quartz substrate. A large number of pine-leaf-shaped microrods (MRs) were obtained. The length of the MRs varied from several to tens of micrometers (Figure S1). From the high-resolution transmission electron microscopy (HRTEM) images and the selected-area electron diffraction (SAED) pattern (Figure 2c), it can be observed the lattice spacing was 0.34 nm, corresponding to the (221) plane of the orthorhombic CsCu<sub>2</sub>I<sub>3</sub> structure. Energy-dispersive spectroscopy (EDS) analysis (Figure 2d) showed the average contents of Cs, Cu,

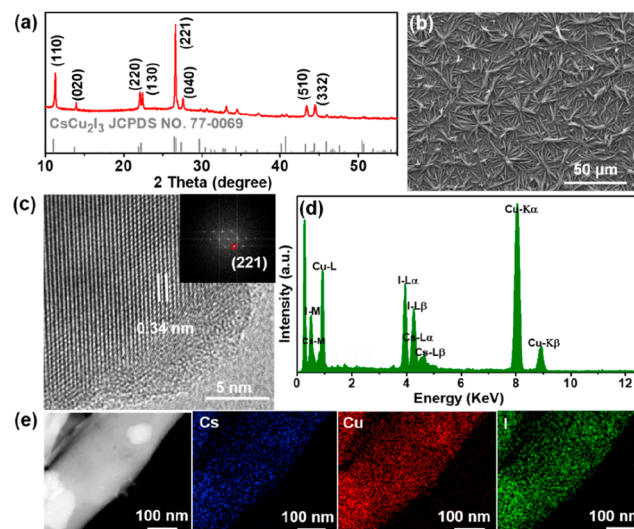


**Figure 2.** (a) XRD pattern and (b) SEM image of the CsCu<sub>2</sub>I<sub>3</sub> film. (c) HRTEM image of CsCu<sub>2</sub>I<sub>3</sub> crystals. The inset is the corresponding fast Fourier transform. (d) EDS spectrum and (e) elemental mapping images of CsCu<sub>2</sub>I<sub>3</sub>.

and I to be 16.32%, 32.91%, and 50.77%, respectively, in agreement with the CsCu<sub>2</sub>I<sub>3</sub> stoichiometry. Figure 2e shows the TEM and elemental mapping images of the CsCu<sub>2</sub>I<sub>3</sub>, which indicate that Cs, Cu, and I were uniformly distributed throughout the MRs. Furthermore, X-ray photoelectron spectroscopy (XPS) was applied to study the chemical nature of CsCu<sub>2</sub>I<sub>3</sub> (Figure S2). The cesium core-level spectrum shows a 3d doublet with an excellent fitting at the binding energies of 723.9 eV (3d<sub>5/2</sub>) and 737.9 eV (3d<sub>3/2</sub>), consistent with Cs<sup>+</sup>.<sup>23,25,26</sup> The copper core-level spectrum shows the Cu 2p<sub>3/2</sub> peak at 931.9 eV and the 2p<sub>1/2</sub> peak at 951.8 eV, corresponding to Cu<sup>+</sup>.<sup>27–29</sup> The iodine core-level spectrum has a 3d doublet with binding energies of 619 eV (3d<sub>5/2</sub>) and 630.3 eV (3d<sub>3/2</sub>), corresponding to I<sup>-</sup>.<sup>17</sup> These results indicate that the CsCu<sub>2</sub>I<sub>3</sub> film possesses high crystallinity.

We further investigated the photophysical properties of the CsCu<sub>2</sub>I<sub>3</sub> film. As shown in the insets of Figure 3a, the CsCu<sub>2</sub>I<sub>3</sub> film is colorless under sunlight and displays bright yellow emission under 254 nm irradiation. The photoluminescence excitation (PLE) and PL spectra of the CsCu<sub>2</sub>I<sub>3</sub> film are presented in Figure 3a. The PL peak is located at 580 nm with a full width at half-maximum (fwhm) of 117 nm, and the PLE peak is at 320 nm. A sharp absorption peak at around 320 nm indicates that the PLE peak is attributed to the excitonic absorption of CsCu<sub>2</sub>I<sub>3</sub>, making it attractive for DUV photodetection.<sup>11,15,30</sup> Meanwhile, the large Stokes shift of 260 nm and broad-band emission signify that the PL emission cannot be ascribed simply to a direct band emission but rather is due to exciton self-trapping from distortion of the lattice.<sup>27,31–33</sup> The PLQY of the CsCu<sub>2</sub>I<sub>3</sub> film was measured to be ~12.3% under 320 nm excitation (Figure 3b), which is comparable to those of the reported low-dimensional lead-free perovskites.<sup>34–36</sup> Figure 3c shows the time-resolved PL decay spectrum of CsCu<sub>2</sub>I<sub>3</sub> film upon 320 nm excitation at room temperature, and the average lifetime is about 86.068 ns on the basis of a fit to a biexponential function. The exciton self-trapping in the 1D perovskite can therefore be depicted as shown in Figure 3d. Upon photoexcitation, the Cu(I) 3d<sup>10</sup> electron configuration changes to Cu(II) 3d<sup>9</sup>, contributing to

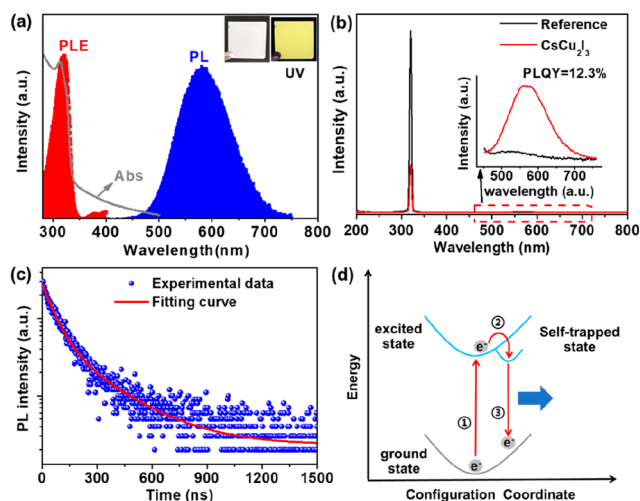


**Figure 3.** (a) Light absorption (gray), PLE (red), and PL (blue) spectra of the CsCu<sub>2</sub>I<sub>3</sub> film. Insets present the (left) bright-field and (right) fluorescence photographs. (b) PLQY and (c) time-resolved PL decay and fitting curves for the CsCu<sub>2</sub>I<sub>3</sub> film. (d) Schematic diagram of free and self-trapped excitons.

Jahn–Teller distortion and the formation of self-trapped excitons, which is similar to the case for the previously reported low-dimensional perovskite.<sup>23,27,37</sup>

The stability of perovskites is one important factor for fabricating photoelectric devices. Therefore, the moisture, thermal, and long-term stabilities of the CsCu<sub>2</sub>I<sub>3</sub> film were tested by tracking the PL intensity variation (Figure 4). The

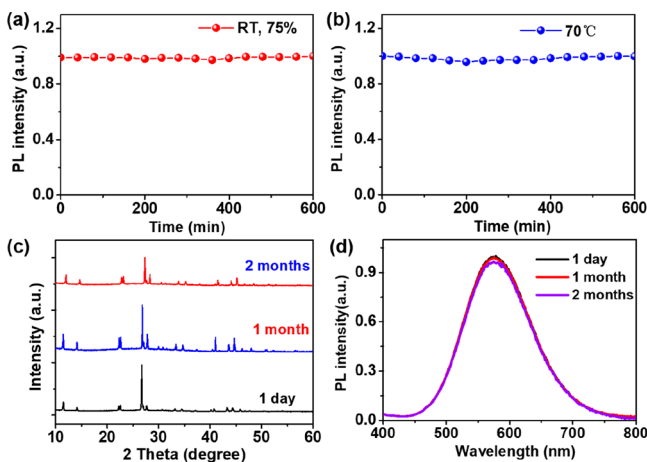


**Figure 4.** Stability of the CsCu<sub>2</sub>I<sub>3</sub> film. (a, b) PL spectra of the CsCu<sub>2</sub>I<sub>3</sub> film (a) under 75% RH environment at room temperature and (b) under a constant temperature at 70 °C. (c) XRD patterns and (d) PL spectra of films stored for several months in an atmospheric environment.

moisture and thermal stability tests were carried by storing the CsCu<sub>2</sub>I<sub>3</sub> film under 75% relative humidity (RH) and a constant temperature at 70 °C, respectively, as shown in Figure 4a,b. Remarkably, the PL intensities of the CsCu<sub>2</sub>I<sub>3</sub> film demonstrate ignorable changes after being kept for 600 min under the 75% RH or 70 °C conditions. In addition, the CsCu<sub>2</sub>I<sub>3</sub> film was stored for several months under an ambient atmosphere to test the long-term stability. As shown in Figure 4c,d, no obvious changes were observed in the XRD results

and the PL intensities of CsCu<sub>2</sub>I<sub>3</sub> film, indicating that the material composition remained intact over the course of several months. All of these results indicate that the CsCu<sub>2</sub>I<sub>3</sub> perovskite has excellent stability.

In order to elucidate the photoluminescence mechanisms of the CsCu<sub>2</sub>I<sub>3</sub> films, the temperature-dependent PL spectra of CsCu<sub>2</sub>I<sub>3</sub> film were measured. As shown in Figure 5a, only one

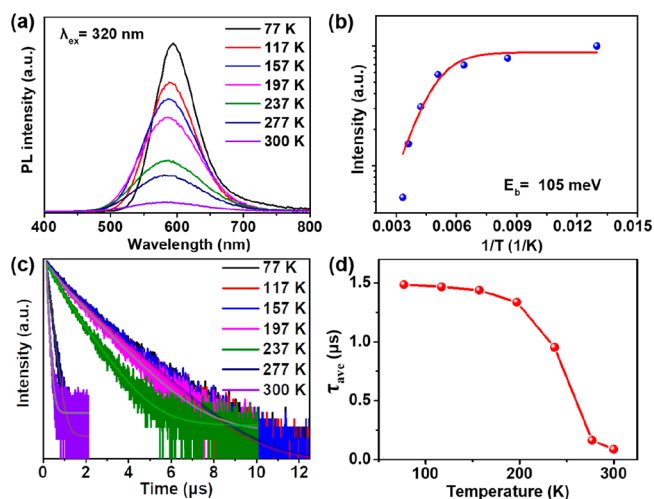


**Figure 5.** (a) Temperature-dependent PL spectra and (b) integrated PL intensities of the CsCu<sub>2</sub>I<sub>3</sub> film. (c) Time-resolved PL decay curves and (d) average lifetimes of the CsCu<sub>2</sub>I<sub>3</sub> film at various temperature.

emission peak can be observed, indicating that no structural phase transition occurs in the investigated temperature region. The position of the PL peak of the CsCu<sub>2</sub>I<sub>3</sub> film slightly redshifts with decreasing temperature following Varshni's model.<sup>38</sup> As expected, the PL intensity decreases with increasing temperature as a result of thermal quenching (Figure 5b). Furthermore, the temperature-dependent PL intensity could be described by eq 1:<sup>39,40</sup>

$$I(T) = \frac{I_0}{1 + A \exp\left(-\frac{E_b}{k_B T}\right)} \quad (1)$$

where  $I(T)$  and  $I_0$  are the integrated PL intensities at temperature  $T$  and 0 K, respectively,  $E_b$  is the exciton binding energy, and  $k_B$  is the Boltzmann constant. From the fitting, we obtained an exciton binding energy of  $\sim 105$  meV, which is much larger than those for 3D Pb-based perovskites (several tens of meV),<sup>41,42</sup> originating from the 1D nature of CsCu<sub>2</sub>I<sub>3</sub>. Additionally, the temperature-dependent PL fwhm (Figure S3) obviously broadens with increasing temperature as a result of the electron–phonon coupling arising from lattice vibrations.<sup>19,43,44</sup> The PL intensity increases and the fwhm narrows as temperature decreases, suggesting that the broad emission does not originate from multiple radiative mechanisms.<sup>45</sup>

To further investigate the recombination dynamics of the CsCu<sub>2</sub>I<sub>3</sub> film, the temperature-dependent time-resolved PL was measured (Figure 5c). The results of the fit to a biexponential function are presented in Table S1. Distinctly, the average lifetime decreases as the temperature increases (Figure 5d), which is the same trend as for the change in PL intensity. It could be speculated that thermal expansion and the interaction between excitons and phonons affect the PL lifetime as a function of temperature. As the temperature



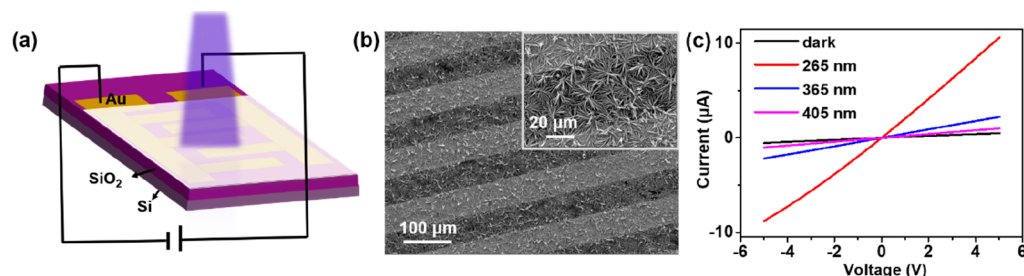


**Figure 6.** (a) Diagram and (b) SEM image of the  $\text{CsCu}_2\text{I}_3$  film device. (c)  $I$ – $V$  characteristics of the  $\text{CsCu}_2\text{I}_3$  film photodetector in the dark and under illumination at various wavelengths.

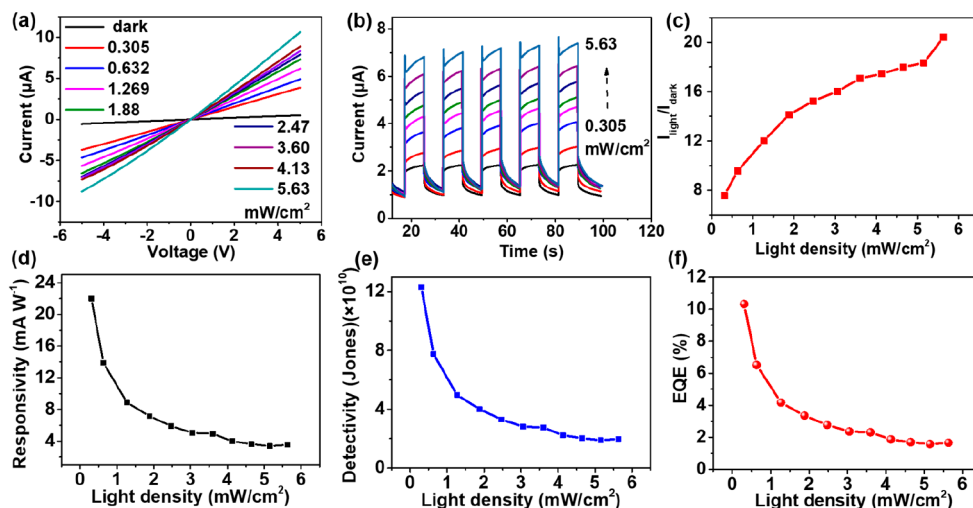


**Figure 7.** (a)  $I$ – $V$  and (b)  $I$ – $t$  characteristics of the  $\text{CsCu}_2\text{I}_3$  film device under 265 nm illumination at different light densities. (c–f)  $I_{\text{light}}/I_{\text{dark}}$  ratio,  $R$ ,  $D^*$ , and EQE, respectively, as functions of the light density.

increases, the lattice vibrations become active and result in energy transfer to the lattice, lowering the radiative recombination.<sup>46</sup>

The  $\text{CsCu}_2\text{I}_3$  film was directly grown on a gold interdigital electrode using an antisolvent-assisted crystallization method. The diagram and SEM image of the  $\text{CsCu}_2\text{I}_3$  film photodetector are portrayed in Figure 6a,b. Figure 6c shows the current–voltage ( $I$ – $V$ ) curves of the device in the dark and under illumination at different wavelengths (265, 365, and 405 nm) at a constant light density (5.63  $\text{mW}/\text{cm}^2$ ). The photocurrent decreases with an increase in the incident light wavelength and is almost zero under 405 nm irradiation, which implies blind photoresponsivity. The dark current is about 0.3  $\mu\text{A}$ , and the current under 265 nm illumination is as high as 6.7  $\mu\text{A}$  at a bias voltage of 3 V. A high  $I_{\text{light}}/I_{\text{dark}}$  ratio of  $\sim 22$  can be achieved at 265 nm, and the  $I_{\text{light}}/I_{\text{dark}}$  ratio under 365 nm illumination was calculated to be 4.3. In contrast, the device is almost insensitive to 405 nm illumination, which is associated with intrinsic absorption property of  $\text{CsCu}_2\text{I}_3$ .

In order to reveal the photoresponse of the  $\text{CsCu}_2\text{I}_3$  film device, we further studied the  $I$ – $V$  curves under 265 nm illumination at different light densities ranging from 0.305 to 5.63  $\text{mW}/\text{cm}^2$  (Figure 7a). The typical symmetrical behavior of the  $I$ – $V$  curves demonstrates good Ohmic contact between the  $\text{CsCu}_2\text{I}_3$  film and the Au electrode.<sup>47,48</sup> Apparently, the photocurrent increased gradually from 2.3 to 6.7  $\mu\text{A}$  with increasing light density at a bias voltage of 3 V, which is attributed to excitation of larger numbers of electron–hole pairs at higher light densities. In addition, the time-dependent

photoresponse was also studied under 265 nm illumination at different light densities (Figure 7b). The  $I_{\text{light}}/I_{\text{dark}}$  ratio of the  $\text{CsCu}_2\text{I}_3$  film device gradually increases with increasing light density, reaching a maximum value of 22 when the light density is increased to 5.63  $\text{mW}/\text{cm}^2$  (Figure 7c). To quantitatively assess the device performance of the  $\text{CsCu}_2\text{I}_3$  film photodetector, several critical parameters were estimated as follows:<sup>30,49–52</sup>

$$R = \frac{I_{\text{light}} - I_{\text{dark}}}{P_{\text{light}} S} \quad (2)$$

$$D^* = \frac{RS^{1/2}}{(2eI_{\text{dark}})^{1/2}} \quad (3)$$

$$\text{EQE} = \frac{Rhc}{e\lambda_{\text{light}}} \quad (4)$$

where  $I_{\text{light}}$  is the photocurrent,  $I_{\text{dark}}$  is the dark current,  $P_{\text{light}}$  is the incident light density,  $S$  is the effective incident area (0.3  $\text{cm}^2$ ),  $e$  is the proton charge,  $h$  is the Planck constant,  $c$  is the speed of light, and  $\lambda_{\text{light}}$  is the wavelength of the incident light. With the above equations, values of  $R$ ,  $D^*$ , and EQE for the  $\text{CsCu}_2\text{I}_3$  film device were estimated at different light densities (Figure 7d–f), and the maximum values of 22.1  $\text{mA}/\text{W}$ ,  $1.2 \times 10^{11}$  Jones, and 10.3% were achieved at a low light density of 0.305  $\text{mW}/\text{cm}^2$ , respectively. Nonetheless, all three parameters decrease gradually with increasing light density, which can be

attributed to the intensified photocurrent recombination loss in the device at high light densities.<sup>48,53</sup>

Besides the light density, the photoresponse of the CsCu<sub>2</sub>I<sub>3</sub> film device was also found to strongly depend upon the bias voltage. Figure S4a shows the  $I-t$  curves of the CsCu<sub>2</sub>I<sub>3</sub> film device under a series of applied bias voltages under the same illumination conditions (light density of 5.63 mW/cm<sup>2</sup> and wavelength of 265 nm). It is noteworthy that the photocurrent gradually increases with rising bias voltage, which is understandable because the larger bias voltage can enhance the drift velocity and separation efficiency of photoexcited electron-hole pairs and therefore suppress the photogenerated carrier recombination.<sup>30,48</sup> We then quantitatively evaluated the photoresponse of device by calculating  $R$  and  $D^*$ . As plotted in Figure S4b, these two parameters increase substantially with rising bias voltage, reaching the maximum values of 6.5 mA/W and  $1.1 \times 10^{10}$  Jones, respectively, at a bias voltage of 3 V. This is reasonable because a high bias voltage can cause an increased probability of exciton separation and acceleration and an enhanced electric field, which will facilitate the photogeneration of more carriers, leading to a higher photocurrent. Significantly, these values are comparable to the values for previously reported photodetectors.<sup>54,55</sup>

In conclusion, we successfully prepared a new nontoxic 1D CsCu<sub>2</sub>I<sub>3</sub> perovskite film via an antisolvent-assisted crystallization method. Benefiting from the 1D crystal structure, strong exciton binding energy (~105 meV), and high crystal quality, the CsCu<sub>2</sub>I<sub>3</sub> film shows excellent stability and a high PLQY of 12.3%. Furthermore, a DUV photodetector based on the CsCu<sub>2</sub>I<sub>3</sub> film was successfully fabricated for the first time and was nearly blind to 405 nm visible light but showed apparent sensitivity to 265 and 365 nm illumination. The device exhibited prominent parameters with excellent reproducibility, and a high  $I_{\text{light}}/I_{\text{dark}}$  ratio of 22 under 265 nm illumination. The  $R$ ,  $D^*$ , and EQE values are as high as 22.1 mA/W,  $1.2 \times 10^{11}$  Jones, and 10.3% under a light density of 0.305 mW/cm<sup>2</sup>. These results corroborate that the CsCu<sub>2</sub>I<sub>3</sub> film DUV photodetector possesses great prospects for use in next-generation optoelectronic devices.

## ■ ASSOCIATED CONTENT

### Supporting Information

The Supporting Information is available free of charge at <https://pubs.acs.org/doi/10.1021/acs.jpcllett.0c01832>.

Materials, methods, and characterizations; length distribution statistics of CsCu<sub>2</sub>I<sub>3</sub> perovskite microrods; XPS spectra; temperature-dependent PL fwhm of the CsCu<sub>2</sub>I<sub>3</sub> film;  $I-t$  curves for the CsCu<sub>2</sub>I<sub>3</sub> film;  $R$  and  $D^*$  at various bias voltages; and fitted PL lifetimes of the CsCu<sub>2</sub>I<sub>3</sub> film (PDF)

## ■ AUTHOR INFORMATION

### Corresponding Authors

**Juan Du** – State Key Laboratory of High Field Laser Physics and CAS Center for Excellence in Ultra-intense Laser Science, Shanghai Institute of Optics and Fine Mechanics, Chinese Academy of Sciences, Shanghai 201800, China; Center of Materials Science and Optoelectronics Engineering and Hangzhou Institute for Advanced Study, University of Chinese Academy of Sciences, Beijing 100049, China; [orcid.org/0000-0003-3221-6810](https://orcid.org/0000-0003-3221-6810); Email: [dujuan@mail.siom.ac.cn](mailto:dujuan@mail.siom.ac.cn)

**Miao Zhou** – Key Laboratory of Optoelectronic Technology & Systems (Ministry of Education), College of Optoelectronic Engineering, Chongqing University, Chongqing 400044, China; Email: [mzhou@cqu.edu.cn](mailto:mzhou@cqu.edu.cn)

**Xiaosheng Tang** – Key Laboratory of Optoelectronic Technology & Systems (Ministry of Education), College of Optoelectronic Engineering, Chongqing University, Chongqing 400044, China; School of Materials Science and Engineering, Zhengzhou University, Zhengzhou 450001, China; [orcid.org/0000-0003-4402-391X](https://orcid.org/0000-0003-4402-391X); Email: [xstang@cqu.edu.cn](mailto:xstang@cqu.edu.cn)

## Authors

**Jie Yang** – Key Laboratory of Optoelectronic Technology & Systems (Ministry of Education), College of Optoelectronic Engineering, Chongqing University, Chongqing 400044, China; College of Physics and Electronic Engineering, Chongqing Normal University, Chongqing 401331, China

**Wei Kang** – Key Laboratory of Optoelectronic Technology & Systems (Ministry of Education), College of Optoelectronic Engineering, Chongqing University, Chongqing 400044, China

**Zhengzheng Liu** – State Key Laboratory of High Field Laser Physics and CAS Center for Excellence in Ultra-intense Laser Science, Shanghai Institute of Optics and Fine Mechanics, Chinese Academy of Sciences, Shanghai 201800, China; Center of Materials Science and Optoelectronics Engineering, University of Chinese Academy of Sciences, Beijing 100049, China

**Mingyu Pi** – College of Physics and Electronic Engineering, Chongqing Normal University, Chongqing 401331, China

**Lin-Bao Luo** – School of Electronic Science and Applied Physics, Hefei University of Technology, Hefei, Anhui 230009, China; [orcid.org/0000-0001-8651-8764](https://orcid.org/0000-0001-8651-8764)

**Chen Li** – School of Electronic Science and Applied Physics, Hefei University of Technology, Hefei, Anhui 230009, China

**Hao Lin** – Key Laboratory of Optoelectronic Technology & Systems (Ministry of Education), College of Optoelectronic Engineering, Chongqing University, Chongqing 400044, China

**Zhongtao Luo** – School of Materials Science and Engineering, Zhengzhou University, Zhengzhou 450001, China

Complete contact information is available at:

<https://pubs.acs.org/doi/10.1021/acs.jpcllett.0c01832>

## Author Contributions

<sup>†</sup>J.Y., W.K., and Z.L. contributed equally to this work.

## Notes

The authors declare no competing financial interest.

## ■ ACKNOWLEDGMENTS

This work was supported by the National Key Research and Development Program of China (2018YFB2200500 and 2017YFE0123700), the National Natural Science Foundation of China (Grants 61975023, 61925507, 61905264, 61875211, 61520106012, and 61674023), the Natural Science Foundation of Chongqing (cstc2019jcyj-msxmX0522), the Science and Technology Research Program of Chongqing Municipal Education Commission (Grant KJQN201900515), the Project of Chongqing Normal University Foundation (Grant 19XWB014), the Chongqing Research Program of Basic Research and Frontier Technology (cstc2018jsz-cyzdX0137), the Strategic Priority Research Program of CAS (XDB16030400), the CAS Interdisciplinary Innovation Team, the Open Fund of the State Key Laboratory of High Field

Laser Physics (Shanghai Institute of Optics and Fine Mechanics), and the Program of Shanghai Academic/Technology Research Leader (18XD1404200).

## REFERENCES

- (1) Kong, W. Y.; Wu, G. A.; Wang, K. Y.; Zhang, T. F.; Zou, Y. F.; Wang, D. D.; Luo, L. B. Graphene-beta-Ga<sub>2</sub>O<sub>3</sub> Heterojunction for Highly Sensitive Deep UV Photodetector Application. *Adv. Mater.* **2016**, *28*, 10725–10731.
- (2) Peng, L.; Hu, L.; Fang, X. Low-Dimensional Nanostructure Ultraviolet Photodetectors. *Adv. Mater.* **2013**, *25*, 5321–5328.
- (3) Razaqhi, M.; Rogalski, A. Semiconductor Ultraviolet Detectors. *J. Appl. Phys.* **1996**, *79*, 7433–7473.
- (4) Sheng, X.; Yu, C.; Malyarchuk, V.; Lee, Y.-H.; Kim, S.; Kim, T.; Shen, L.; Horng, C.; Lutz, J.; Giebink, N. C.; et al. Silicon-Based Visible-Blind Ultraviolet Detection and Imaging Using Down-Shifting Luminophores. *Adv. Opt. Mater.* **2014**, *2*, 314–319.
- (5) Taniyasu, Y.; Kasu, M.; Makimoto, T. An Aluminium Nitride Light-emitting Diode With a Wavelength of 210 Nanometres. *Nature* **2006**, *441*, 325–328.
- (6) Razaqhi, M. Short-Wavelength Solar-Blind Detectors—Status, Prospects, and Markets. *P. Proc. IEEE* **2002**, *90*, 1006–1014.
- (7) Li, Y.; Tokizono, T.; Liao, M.; Zhong, M.; Koide, Y.; Yamada, I.; Delaunay, J.-J. Efficient Assembly of Bridged  $\beta$ -Ga<sub>2</sub>O<sub>3</sub> Nanowires for Solar-Blind Photodetection. *Adv. Funct. Mater.* **2010**, *20*, 3972–3978.
- (8) Tut, T.; Yelboga, T.; Ulker, E.; Ozbay, E. Solar-blind AlGaIn-based p-i-n Photodetectors with High Breakdown Voltage and Detectivity. *Appl. Phys. Lett.* **2008**, *92*, 103502.
- (9) Xie, C.; Lu, X.-T.; Tong, X.-W.; Zhang, Z.-X.; Liang, F.-X.; Liang, L.; Luo, L.-B.; Wu, Y.-C. Recent Progress in Solar-Blind Deep-Ultraviolet Photodetectors Based on Inorganic Ultrawide Bandgap Semiconductors. *Adv. Funct. Mater.* **2019**, *29*, 1806006.
- (10) Zhao, B.; Wang, F.; Chen, H.; Wang, Y.; Jiang, M.; Fang, X.; Zhao, D. Solar-Blind Avalanche Photodetector Based on Single ZnO-Ga<sub>2</sub>O<sub>3</sub> Core-Shell Microwire. *Nano Lett.* **2015**, *15*, 3988–93.
- (11) Adinolfi, V.; Ouellette, O.; Saidaminov, M. I.; Walters, G.; Abdelhady, A. L.; Bakr, O. M.; Sargent, E. H. Fast and Sensitive Solution-Processed Visible-Blind Perovskite UV Photodetectors. *Adv. Mater.* **2016**, *28*, 7264–7268.
- (12) Gong, J.; Li, X.; Guo, P.; Zhang, L.; Huang, W.; Lu, K.; Cheng, Y.; Schaller, R. D.; Marks, T. J.; Xu, T. Energy-distinguishable bipolar UV Photoelectron Injection from LiCl-promoted FAPbCl<sub>3</sub> Perovskite Nanorods. *J. Mater. Chem. A* **2019**, *7*, 13043–13049.
- (13) Gui, P.; Zhou, H.; Yao, F.; Song, Z.; Li, B.; Fang, G. Space-Confined Growth of Individual Wide Bandgap Single Crystal CsPbCl<sub>3</sub> Microplatelet for Near-Ultraviolet Photodetection. *Small* **2019**, *15*, 1902618.
- (14) Lu, J.; Sheng, X.; Tong, G.; Yu, Z.; Sun, X.; Yu, L.; Xu, X.; Wang, J.; Xu, J.; Shi, Y.; et al. Ultrafast Solar-Blind Ultraviolet Detection by Inorganic Perovskite CsPbX<sub>3</sub> Quantum Dots Radial Junction Architecture. *Adv. Mater.* **2017**, *29*, 1700400.
- (15) Maculan, G.; Sheikh, A. D.; Abdelhady, A. L.; Saidaminov, M. I.; Haque, M. A.; Murali, B.; Alarousu, E.; Mohammed, O. F.; Wu, T.; Bakr, O. M. CH<sub>3</sub>NH<sub>3</sub>PbCl<sub>3</sub> Single Crystals: Inverse Temperature Crystallization and Visible-Blind UV-Photodetector. *J. Phys. Chem. Lett.* **2015**, *6*, 3781–3786.
- (16) Yang, L.; Tsai, W. L.; Li, C. S.; Hsu, B. W.; Chen, C. Y.; Wu, C. I.; Lin, H. W. High-Quality Conformal Homogeneous All-Vacuum Deposited CsPbCl<sub>3</sub> Thin Films and their UV Photodiode Applications. *ACS Appl. Mater. Interfaces* **2019**, *11*, 47054–47062.
- (17) Cheng, P.; Sun, L.; Feng, L.; Yang, S.; Yang, Y.; Zheng, D.; Zhao, Y.; Sang, Y.; Zhang, R.; Wei, D.; et al. Colloidal Synthesis and Optical Properties of All-Inorganic Low-Dimensional Cesium Copper Halide Nanocrystals. *Angew. Chem., Int. Ed.* **2019**, *58*, 16087–16091.
- (18) Hull, S.; Berastegui, P. Crystal Structures and Ionic Conductivities of Ternary Derivatives of the Silver and Copper Monohalides—II: Ordered phases within the (AgX)<sub>x</sub>–(MX)<sub>1–x</sub> and (CuX)<sub>x</sub>–(MX)<sub>1–x</sub> (M = K, Rb and Cs; X = Cl, Br and I) systems. *J. Solid State Chem.* **2004**, *177*, 3156–3173.
- (19) Rocanova, R.; Yangui, A.; Seo, G.; Creason, T. D.; Wu, Y.; Kim, D. Y.; Du, M.-H.; Saparov, B. Bright Luminescence from Nontoxic CsCu<sub>2</sub>X<sub>3</sub> (X = Cl, Br, I). *ACS Mater. Lett.* **2019**, *1*, 459–465.
- (20) Dong, C.; Han, X.; Li, W.; Qiu, Q.; Wang, J. Anti-solvent Assisted Multi-step Deposition for Efficient and Stable Carbon-based CsPbI<sub>2</sub>Br All-Inorganic Perovskite Solar Cell. *Nano Energy* **2019**, *59*, 553–559.
- (21) Zhang, X.; Wang, W.; Xu, B.; Liu, S.; Dai, H.; Bian, D.; Chen, S.; Wang, K.; Sun, X. W. Thin Film Perovskite Light-Emitting Diode Based on CsPbBr<sub>3</sub> Powders and Interfacial Engineering. *Nano Energy* **2017**, *37*, 40–45.
- (22) Cho, H.; Jeong, S.-H.; Park, M.-H.; Kim, Y.-H.; Wolf, C.; Lee, C.-L.; Heo, J. H.; Sadhanala, A.; Myoung, N.; Yoo, S.; et al. Overcoming the Electroluminescence Efficiency limitations of perovskite light-emitting diodes. *Science* **2015**, *350*, 1222–1225.
- (23) Lin, R.; Guo, Q.; Zhu, Q.; Zhu, Y.; Zheng, W.; Huang, F. All-Inorganic CsCu<sub>2</sub>I<sub>3</sub> Single Crystal with High-PLQY (approximately 15.7%) Intrinsic White-light Emission Via Strongly Localized 1D Excitonic Recombination. *Adv. Mater.* **2019**, *31*, 1905079.
- (24) Cheng, P.; Sun, L.; Feng, L.; Yang, S.; Yang, Y.; Zheng, D.; Zhao, Y.; Sang, Y.; Zhang, R.; Wei, D.; et al. Colloidal Synthesis and Optical Properties of All-Inorganic Low-Dimensional Cesium Copper Halide Nanocrystals. *Angew. Chem.* **2019**, *131*, 16233–16237.
- (25) Yang, J.; Liu, Z.; Zeng, F.; Pi, M.; Shi, T.; Bian, Y.; Tang, X.; Du, J.; Liu, W.; Leng, Y. High-Quality Single-Mode Lasers Based on Zero-Dimensional Cesium Lead Halide Perovskites. *Sol. RRL* **2019**, *3*, 1900127.
- (26) Tang, X.; Yang, J.; Li, S.; Liu, Z.; Hu, Z.; Hao, J.; Du, J.; Leng, Y.; Qin, H.; Lin, X.; et al. Single Halide Perovskite/Semiconductor Core/Shell Quantum Dots with Ultraprobability and Nonblinking Properties. *Adv. Sci.* **2019**, *6*, 1900412.
- (27) Yang, B.; Yin, L.; Niu, G.; Yuan, J. H.; Xue, K. H.; Tan, Z.; Miao, X. S.; Niu, M.; Du, X.; Song, H.; et al. Lead-Free Halide Rb<sub>2</sub>CuBr<sub>3</sub> as Sensitive X-ray Scintillator. *Adv. Mater.* **2019**, *31*, 1904711.
- (28) Su, H.; Xie, Y.; Wan, S.; Li, B.; Qian, Y. A Novel One-step Solvothermal Route to Nanocrystalline CuSb<sub>2</sub>S<sub>3</sub> and Ag<sub>3</sub>SbS<sub>3</sub>. *Solid State Ionics* **1999**, *123*, 319–324.
- (29) Li, Z.; Li, Z.; Shi, Z.; Fang, X. Facet-Dependent, Fast Response, and Broadband Photodetector Based on Highly Stable All-Inorganic CsCu<sub>2</sub>I<sub>3</sub> Single Crystal with 1D Electronic Structure. *Adv. Funct. Mater.* **2020**, 2002634.
- (30) Zhang, Z. X.; Li, C.; Lu, Y.; Tong, X. W.; Liang, F. X.; Zhao, X. Y.; Wu, D.; Xie, C.; Luo, L. B. Sensitive Deep Ultraviolet Photodetector and Image Sensor Composed of Inorganic Lead-Free Cs<sub>3</sub>Cu<sub>2</sub>I<sub>5</sub> Perovskite with Wide Bandgap. *J. Phys. Chem. Lett.* **2019**, *10*, 5343–5350.
- (31) Li, S.; Luo, J.; Liu, J.; Tang, J. Self-Trapped Excitons in All-Inorganic Halide Perovskites: Fundamentals, Status, and Potential Applications. *J. Phys. Chem. Lett.* **2019**, *10*, 1999–2007.
- (32) Rocanova, R.; Yangui, A.; Nhalil, H.; Shi, H.; Du, M.-H.; Saparov, B. Near-Unity Photoluminescence Quantum Yield in Blue-Emitting Cs<sub>3</sub>Cu<sub>2</sub>Br<sub>5–x</sub>I<sub>x</sub> (0 ≤ x ≤ 5). *ACS Appl. Electron. Mater.* **2019**, *1*, 269–274.
- (33) Luo, Z.; Li, Q.; Zhang, L.; Wu, X.; Tan, L.; Zou, C.; Liu, Y.; Quan, Z. 0D Cs<sub>3</sub>Cu<sub>2</sub>X<sub>5</sub> (X = I, Br, and Cl) Nanocrystals: Colloidal Syntheses and Optical Properties. *Small* **2020**, *16*, 1905226.
- (34) Wu, G.; Zhou, C.; Ming, W.; Han, D.; Chen, S.; Yang, D.; Besara, T.; Neu, J.; Siegrist, T.; Du, M.-H.; et al. A One-Dimensional Organic Lead Chloride Hybrid with Excitation-Dependent Broadband Emissions. *ACS Energy Lett.* **2018**, *3*, 1443–1449.
- (35) Liu, Y.; Jing, Y.; Zhao, J.; Liu, Q.; Xia, Z. Design Optimization of Lead-Free Perovskite Cs<sub>2</sub>AgInCl<sub>6</sub>:Bi Nanocrystals with 11.4% Photoluminescence Quantum Yield. *Chem. Mater.* **2019**, *31*, 3333–3339.



- (36) Dohner, E. R.; Jaffe, A.; Bradshaw, L. R.; Karunadasa, H. I. Intrinsic White-light Emission from Layered Hybrid Perovskites. *J. Am. Chem. Soc.* **2014**, *136*, 13154–7.
- (37) Li, Y.; Shi, Z.; Wang, L.; Chen, Y.; Liang, W.; Wu, D.; Li, X.; Zhang, Y.; Shan, C.; Fang, X. Solution-processed One-dimensional  $\text{CsCu}_2\text{I}_3$  Nanowires for Polarization-sensitive and Flexible Ultraviolet Photodetectors. *Mater. Horiz.* **2020**, *7*, 1613–1622.
- (38) Fan, H. Y. Temperature Dependence of the Energy Gap in Semiconductors. *Phys. Rev.* **1951**, *82*, 900–905.
- (39) Liu, Z.; Yang, J.; Du, J.; Hu, Z.; Shi, T.; Zhang, Z.; Liu, Y.; Tang, X.; Leng, Y.; Li, R. Robust Subwavelength Single-Mode Perovskite Nanocuboid Laser. *ACS Nano* **2018**, *12*, 5923–5931.
- (40) Chen, Z.; Yu, C.; Shum, K.; Wang, J. J.; Pfenninger, W.; Vockic, N.; Midgley, J.; Kenney, J. T. Photoluminescence Study of Polycrystalline  $\text{CsSnI}_3$  Thin Films: Determination of Exciton Binding Energy. *J. Lumin.* **2012**, *132*, 345–349.
- (41) Li, X.; Wu, Y.; Zhang, S.; Cai, B.; Gu, Y.; Song, J.; Zeng, H.  $\text{CsPbX}_3$  Quantum Dots for Lighting and Displays: Room-Temperature Synthesis, Photoluminescence Superiorities, Underlying Origins and White Light-Emitting Diodes. *Adv. Funct. Mater.* **2016**, *26*, 2435–2445.
- (42) Savenije, T. J.; Ponseca, C. S., Jr.; Kunneman, L.; Abdellah, M.; Zheng, K.; Tian, Y.; Zhu, Q.; Canton, S. E.; Scheblykin, I. G.; Pullerits, T.; et al. Thermally Activated Exciton Dissociation and Recombination Control the Carrier Dynamics in Organometal Halide Perovskite. *J. Phys. Chem. Lett.* **2014**, *5*, 2189–2194.
- (43) Wright, A. D.; Verdi, C.; Milot, R. L.; Eperon, G. E.; Pérez-Osorio, M. A.; Snaith, H. J.; Giustino, F.; Johnston, M. B.; Herz, L. M. Electron–Phonon Coupling in Hybrid Lead Halide Perovskites. *Nat. Commun.* **2016**, *7*, 11755.
- (44) Li, Y.; Shi, Z.; Liang, W.; Wang, L.; Li, S.; Zhang, F.; Ma, Z.; Wang, Y.; Tian, Y.; Wu, D.; et al. Highly Stable and Spectrum-selective Ultraviolet Photodetectors Based on Lead-free Copper-based Perovskites. *Mater. Horiz.* **2020**, *7*, 530–540.
- (45) Zhou, L.; Liao, J. F.; Huang, Z. G.; Wei, J. H.; Wang, X. D.; Li, W. G.; Chen, H. Y.; Kuang, D. B.; Su, C. Y. A Highly Red-Emissive Lead-Free Indium-Based Perovskite Single Crystal for Sensitive Water Detection. *Angew. Chem., Int. Ed.* **2019**, *58*, 5277–5281.
- (46) Du, W.; Zhang, S.; Wu, Z.; Shang, Q.; Mi, Y.; Chen, J.; Qin, C.; Qiu, X.; Zhang, Q.; Liu, X. Unveiling Lasing Mechanism in  $\text{CsPbBr}_3$  Microsphere Cavities. *Nanoscale* **2019**, *11*, 3145–3153.
- (47) Ji, C.; Wang, P.; Wu, Z.; Sun, Z.; Li, L.; Zhang, J.; Hu, W.; Hong, M.; Luo, J. Inch-Size Single Crystal of a Lead-Free Organic-Inorganic Hybrid Perovskite for High-Performance Photodetector. *Adv. Funct. Mater.* **2018**, *28*, 1705467.
- (48) Liang, F. X.; Zhao, X. Y.; Jiang, J. J.; Hu, J. G.; Xie, W. Q.; Lv, J.; Zhang, Z. X.; Wu, D.; Luo, L. B. Light Confinement Effect Induced Highly Sensitive, Self-Driven Near-Infrared Photodetector and Image Sensor Based on Multilayer  $\text{PdSe}_2$  /Pyramid Si Heterojunction. *Small* **2019**, *15*, 1903831.
- (49) Wu, D.; Wang, Y.; Zeng, L.; Jia, C.; Wu, E.; Xu, T.; Shi, Z.; Tian, Y.; Li, X.; Tsang, Y. H. Design of 2D Layered  $\text{PtSe}_2$  Heterojunction for the High-Performance, Room-Temperature, Broadband, Infrared Photodetector. *ACS Photonics* **2018**, *5*, 3820–3827.
- (50) Zhou, J.; Huang, J. Photodetectors Based on Organic-Inorganic Hybrid Lead Halide Perovskites. *Adv. Sci.* **2018**, *5*, 1700256.
- (51) Deng, W.; Zhang, X.; Huang, L.; Xu, X.; Wang, L.; Wang, J.; Shang, Q.; Lee, S. T.; Jie, J. Aligned Single-Crystalline Perovskite Microwire Arrays for High-Performance Flexible Image Sensors with Long-Term Stability. *Adv. Mater.* **2016**, *28*, 2201–2208.
- (52) Xie, C.; Yan, F. Flexible Photodetectors Based on Novel Functional Materials. *Small* **2017**, *13*, 1701822.
- (53) Boruah, B. D.; Mukherjee, A.; Misra, A. Sandwiched Assembly of  $\text{ZnO}$  Nanowires between Graphene Layers for a Self-powered and Fast Responsive Ultraviolet Photodetector. *Nanotechnology* **2016**, *27*, 095205.
- (54) Wu, Y.; Chang, S.-J.; Weng, W.; Liu, C.; Tsai, T.; Hsu, C.; Chen, K.  $\text{Ga}_2\text{O}_3$  Nanowire Photodetector Prepared on  $\text{SiO}_2$ /Si Template. *IEEE Sens. J.* **2013**, *13*, 2368–2373.
- (55) Cheng, X.; Jing, L.; Zhao, Y.; Du, S.; Ding, J.; Zhou, T. Crystal Orientation-dependent Optoelectronic Properties of  $\text{MAPbCl}_3$  Single Crystals. *J. Mater. Chem. C* **2018**, *6*, 1579–1586.